



# Activated carbon prepared from hazelnut shell waste and magnetized by Fe<sub>3</sub>O<sub>4</sub> nanoparticles for highly efficient adsorption of fluoride

Tariq J. Al-Musawi<sup>1</sup> · Gordon McKay<sup>2</sup> · Abdullah Kadhim<sup>1</sup> · Maryam Masoumi Joybari<sup>3</sup> · Davoud Balarak<sup>4</sup>

Received: 17 January 2022 / Revised: 1 March 2022 / Accepted: 12 March 2022 / Published online: 25 March 2022  
© The Author(s), under exclusive licence to Springer-Verlag GmbH Germany, part of Springer Nature 2022

## Abstract

This study involved the preparation of magnetized activated carbon (Fe<sub>3</sub>O<sub>4</sub>-HSAC) by first activating hazelnut shell waste, followed by coating it by Fe<sub>3</sub>O<sub>4</sub> nanoparticles. The Fe<sub>3</sub>O<sub>4</sub>-HSAC thus prepared was evaluated as an adsorbent possessing the potential for fluoride to elimination, under a variety of conditions. From the findings, it is evident that by using the Fe<sub>3</sub>O<sub>4</sub>-HSAC as an adsorbent 100% fluoride removal could be accomplished under the optimum conditions cited (adsorbent dose = 0.75 g/L; pH = 3–5; and temperature = 323 K). The Halsey and Freundlich isotherm models both concurred strongly with the equilibrium adsorption data, and from the results of the Langmuir model, the maximum adsorption capacity was achieved at 146.2 mg/g when the temperature was 298 K and pH was 5. The pseudo-second-order kinetic model offered the best explanation for the adsorption process. Besides, both the intra-particle diffusion and liquid film diffusion models were found to control the kinetic mechanism of the fluoride adsorption onto the Fe<sub>3</sub>O<sub>4</sub>-HSAC. The quantity of adsorption energy provided using the Dubinin–Radushkevich model was 4.59 kJ/mol, indicating that the physical adsorption was predominant. Further, the negative values of Gibbs free energy change ( $\Delta G^\circ = -2.73$  to  $-8.11$  kJ/mol at temperature = 288 to 318 K, respectively) and the positive values of enthalpy change ( $\Delta H^\circ = 56.01$  kJ/mol) and entropy change ( $\Delta S^\circ = 0.198$  kJ/mol. K) suggest that the nature of the adsorption thermodynamics is endothermic, spontaneous, and physical. From this study, the observation of the outstanding performance of the Fe<sub>3</sub>O<sub>4</sub>-HSAC helped to conclude that this is a material of promise as a treatment agent in the fluoride elimination from contaminated water and wastewater.

**Keywords** Fe<sub>3</sub>O<sub>4</sub>-HSAC · Fluoride adsorption · Kinetic · Isotherm · Models · Error function

## 1 Introduction

Among the natural elements present in profusion in the rocks composing the crust of the earth, fluoride is also found in significant quantities in the water bodies of many

regions around the globe, due to the indiscriminate disposal of industrial, weathering, and geochemical dissolution of fluoride-rich rocks into aquatic environments [1, 2]. Fluoride gains easy entry into the human body via various sources, namely water, food, air, medicine, and cosmetics [3]. The commonest fluoride source, however, is drinking water. Based on the dosage and length of exposure, fluoride exerts both favorable and injurious effects on human health [4]. According to the WHO, fluoride levels in drinking water should not exceed 1.5 mg/L [5]. For both humans and animals, fluoride is crucial, only in small quantities, for the prevention of tooth decay and in the building of good bone structure [6]. For human beings, it is accepted as a micro-nutrient as it prevents tooth decay. However, high fluoride doses, based on its concentration in the drinking water, can induce fluorosis, both dental and skeletal [7–10].

The rural areas of developing countries clearly reveal fluorosis as a health hazard, especially where the economies are poorly developed and the issue of unsafe

✉ Davoud Balarak  
dbalarak2@gmail.com

<sup>1</sup> Building and Construction Techniques Engineering Department, Al-Mustaqbal University College, 51001 Hillah, Babylon, Iraq

<sup>2</sup> Division of Sustainable Development, College of Science and Engineering, Hamad Bin Khalifa University, Education City, Doha, Qatar

<sup>3</sup> Student Research Committee, Zahedan University of Medical Sciences, Zahedan, Iran

<sup>4</sup> Department of Environmental Health, Health Promotion Research Center, University of Medical Sciences, Zahedan, Iran

drinking water has escalated due to technological challenges [11, 12]. Therefore, for many countries, lowering the fluoride concentration to less than the WHO-stipulated limit, through the expansion of inexpensive and environment friendly anti-fluoridation technologies, is very significant [13, 14]. Hence, several techniques have been employed to achieve fluoride removal, including adsorption via the use of activated alumina, alum, ash, ion exchange resins, and membrane processes, such as ion exchange and electrodialysis, precipitation/coagulation, and chemical precipitation; however, a majority of these methods involve drawbacks such as expensive maintenance and operation expenditure, secondary pollution, and complex treatment methods that are tough to employ. Membrane separation principally involves the reverse osmosis and nanofiltration processes [15, 16]. Although very high purity water can be produced this way, the high energy consumption and membrane deposition are the main disadvantages. During electrodialysis, the electrical potential of the fluoride ions facilitates their transportation through the semipermeable membrane, an expensive process which is also easily influenced by other soluble ions [17].

In the community, fluoride removal is accomplished by adsorption, the favored method because it is inexpensive, easy to operate, highly efficient, and convenient to access, besides being environmentally benign. It also does not demand operational skills or the use of electricity for its performance and includes the advantage of reusing and recycling the adsorbents. This makes it ideal for use in the rural areas of less developed regions of the world [18]. Another benefit is that it can be employed in a water supply system which is decentralized. As various adsorbents are available in large amounts and are very affordable, they are potential candidates for fluoride elimination in distant locations [19].

In water and wastewater treatments, the most extensively used adsorbent is commercially activated carbon. It possesses the outstanding properties of having a large area, high porosity, and a chemical nature. However, because it is expensive, efforts have been directed at exploring a variety of cost-effective materials to produce activated carbon. From among several options, greater attention has been paid, in the recent years, to agricultural wastes as they are widely available in large amounts and are very economical [19]. In fact, agricultural wastes mostly contain lignin and cellulose, besides other composites, including the functional groups such as alcohols, aldehydes, ketones, carboxylates, phenols, and ethers [20]. These groups absorb the hydrogen ions and replace them with the ions present in the solution or by donating an electron pair to form a complex with the ions in the solution. As agricultural wastes possess fibers

and have high porosity and low molecular weight, they can be used as effective and inexpensive adsorbents in contaminant elimination [19]. In this study, the focus was on preparing and producing activated carbon from the waste shells of the hazelnut (*Corylus avellana*), as they are always discarded as solid wastes, in many regions around the globe. From the reports available, it is evident that the global, annual production of hazelnuts is one million and one hundred thousand tons. In fact, Iran stands sixth in the world for the production of this nut, registering an output of thirty-one thousand tons. Therefore, from an environmental perspective, the production of activated carbon will be a good solution for one of the biggest environmental issues, namely the processes of agricultural waste collection and its disposal [21, 22].

In recent times, the coating of adsorbents with magnetic nanoparticles was investigated to raise the adsorption capacity and to promote its recovery value from aqueous media [23–25]. Tran et al. have examined the adsorption removal of methylene blue (MB) from wastewater by using magnetic  $\text{Fe}_3\text{O}_4$ /zeolite NaA nanocomposite ( $\text{Fe}_3\text{O}_4$ /ZA). They found that the removal efficiency and the adsorption capacity were increased rapidly with  $\text{Fe}_3\text{O}_4$  loading ( $\sim 3.3$ – $9.3\%$  wt.) in the  $\text{Fe}_3\text{O}_4$ /ZA composition [26]. In fact, one of the most economically and operationally significant factors is the separation of the spent activated carbon at the culmination of the treatment process, particularly in the adsorption treatment systems. As an effective solution to the separation issue, as well as a means to boost the removal efficiency through extending the surface area, magnetization of the adsorbent used has been identified as a technique of great promise. Magnetization of the activated carbon with the  $\text{Fe}_3\text{O}_4$  magnetic nanoparticle coating revealed a powerful effect on raising both the adsorption capacity and action of the coated activated carbon when contrasted with the non-coated activated carbon [18, 19].

Therefore, the aim of the current study is to synthesize activated carbon derived from the shell waste of hazelnut, as an effective adsorbent, after magnetizing it by coating it with  $\text{Fe}_3\text{O}_4$  magnetic nanoparticles. Evaluation of the synthesized adsorbent ( $\text{Fe}_3\text{O}_4$ -HSAC) was done for the elimination of the fluoride residuals present in water bodies. The adsorption capacity and mechanism were assessed in terms of the isotherm, kinetics, and thermodynamic studies. The removal efficiency of fluoride by the adsorbent employed was investigated for different values of pH, contact time, initial fluoride concentration, and adsorbent concentration, using batch experiments. For five sequential fluoride adsorption-desorption cycles, the degree of regeneration was estimated. Besides, using advanced characterization techniques, the structural and morphological properties were studied.

## 2 Materials and methods

### 2.1 Chemicals

Sodium fluoride anhydrous (99%), 0.1 M hydrochloric acid (36.5%), sodium hydroxide ( $\geq 98\%$ ), SPADNS reagent (90%), zirconium acid (30%), and  $\text{ZnCl}_2$  (28%) were procured from Merck Company. The  $\text{FeCl}_2 \cdot 4\text{H}_2\text{O}$  ( $\geq 99\%$ ) and  $\text{FeCl}_3 \cdot 6\text{H}_2\text{O}$  ( $> 98\%$ ) were supplied by Sigma–Aldrich Company. First, 2.21 g of sodium fluoride anhydrous was dissolved in distilled water in a volumetric flask (1 L) to prepare the 1000 mg/L stock solution of sodium fluoride (NaF), which was diluted to a specific degree. Other standard fluoride solutions were prepared, in the concentrations essential to calibrate the fluoride ion-selective electrode (FISE), through successive dilutions of the stock solution, by adding distilled water.

### 2.2 Preparation of adsorbent

Using the chemical precipitation method, the preparation of the  $\text{Fe}_3\text{O}_4$  nanoparticles was carefully done [18]. First, 80 mm of 0.2 M solution of  $\text{FeCl}_3 \cdot 6\text{H}_2\text{O}$  and 0.1 M  $\text{FeCl}_2 \cdot 4\text{H}_2\text{O}$  were mixed in a flask, in a 2:1 ratio by volume. Next, 10%  $\text{NH}_4\text{OH}$  solution was added to the mixture, and for one hour, the reaction was left to continue, at room temperature until the pH reached 10 and the solution color changed to black. The precipitate ( $\text{Fe}_3\text{O}_4$  nanoparticles) was then drawn out with the help of a super magnet bar. Finally, this was washed many times using deionized water.

Simultaneously, to produce the activated carbon, hazelnut shells were gathered from local sources in northern Iran. The first step involved washing the hazelnut shells several times using distilled water to ensure removal of the surface impurities. Next, after it was dried at 105 °C, it was crushed and sieved in a hammer mill. For the production of activated carbon, 5 g of hazelnut shell was mixed with 40 ml of 28%  $\text{ZnCl}_2$  for 6 h, on a shaker, set at a speed of 120 rpm. Then, the microns were filtered through a 0.45- $\mu\text{m}$  membrane and dried at once at 105 °C for 24 h. The resultant mixture was placed in a vertical furnace, under inert atmosphere, at 650 °C temperature for 1 h, in the presence of nitrogen passed in at 300 ml/min flow rate and 10° C 1/min heat rate. The activated carbon thus produced was washed well with 0.05 M HCl and distilled water ensuring that the residual  $\text{ZnCl}_2$  was removed; this was continued until the leached solution reached neutral pH (between 6 and 7). Finally, it was dried under 110 °C temperature for 24 h and stored in a desiccator (termed HSAC here).

The  $\text{Fe}_3\text{O}_4$ -HSAC was prepared by mixing 4 g of HSAC with 20 ml of 1 M nitric acid solution. This was placed in an ultrasonic bath at 80 °C for 3 h, after which it was passed through 0.45-micron filter and then dried immediately at 105 °C for 6 h. Next, 3 g of carbon was added to 200 ml of deionized water and 2 g of the  $\text{Fe}_3\text{O}_4$  nanoparticles was mixed into this solution. Now, this was placed in an ultrasound bath at 80 °C for one hour. The adsorbent was first subjected to one wash in 200 ml of ethanol and then washed and filtered three successive times with distilled water. Finally, it was dried immediately at 100 °C for 24 h.

### 2.3 Characterization analysis

The crystal structure of the adsorbent used in this work was studied under X-ray diffraction spectroscopy (XRD, PW1730 model, Philips) in which the Cu-K $\alpha$  radiation source was in the 2-theta range (20–70° range). Using TEM analysis, the adsorbent employed was determined using the LEO 912 AB model. The surface physical morphologies of the HSAC and  $\text{Fe}_3\text{O}_4$ -HSAC were inspected with the help of the SEM/EDX (Mira 3-XMU model). The measurements of the FTIR spectra were taken in the 4000–400  $\text{cm}^{-1}$  range, using 8 scans at 4  $\text{cm}^{-1}$  resolution, adopting the KBr pellet method, by a Thermo Nicolet AVATAR 5700. A surface-area analyzer (ASAP2020, USA) helped to identify the specific surface area and pore-size distribution, while the relevant indices were assessed through the Brunauer–Emmett–Teller (BET) and Barrett–Joyner–Halenda (BJH) analysis, respectively. A vibrating sample was used to estimate the magnetic responses of the  $\text{Fe}_3\text{O}_4$ -HSAC and  $\text{Fe}_3\text{O}_4$  (Micromeritics Instrument Corp., Norcross, GA, USA) with an applied force between -8000 and 8000 Oe, at room temperature.

### 2.4 Experiments

Adsorption and defluoridation were carefully scrutinized for optimization of the different parameters selected in these experiments, including contact time, initial fluoride concentration, adsorbent dose, and pH, all of which have the ability to influence the efficiency of the fluoride adsorption on the  $\text{Fe}_3\text{O}_4$ -HSAC. The batch system was adopted to study the adsorption by stirring 0.5 g/L of the adsorbent in 100 ml of 10 mg/L fluoride solution, in 250-ml plastic bottles, keeping the pH at 5, for 90 min. A stirrer with a hot plate was used to stir the fluoride solutions, at room temperature. Adjustments were made to the pH as desired, by the addition of 0.1 M NaOH or 0.1 M HCl. To detect any likelihood of errors, all the tests were done in two steps. Therefore, a final count of 64 samples was involved, keeping in line with the parameter

optimality and repetition of the experiments. In order to achieve accuracy, the fluoride electrode selected was calibrated prior to every experiment. Calibration of the pH meter was performed for each measurement, with the help of pH calibration buffers. Maintaining the temperature at  $25 \pm 2^\circ \text{C}$ , all the experiments were completed. The calibration curve was achieved using different fluoride concentrations prepared from 100 mg/L of the stock solution. Each of the samples prepared was studied by adding 1 ml of zirconium acid reagent and 1 ml of SPADNS reagent. Once the color change was observed, the samples were subjected to testing for fluoride content, at 570 nm, employing the UV–Vis spectrophotometer (DR5000, Hach). Finally, based on the following equations, the adsorption capacity (uptake) and removal efficiency of the  $\text{Fe}_3\text{O}_4$ –HSAC for fluoride were assessed [27, 28].

$$q_e = \frac{(C_0 - C_e)V}{M} \quad (1)$$

$$\% \text{ Removal} = \frac{(C_0 - C_e) \times 100}{C_0} \quad (2)$$

where  $q_e$  (mg/g) refers to the fluoride uptake capacity observed at equilibrium,  $C_0$  and  $C_e$  (mg/L) indicate the starting and residual fluoride concentrations,  $V$  (mL) implies the sample volume, and  $M$  (mg) represents the quantity of the  $\text{Fe}_3\text{O}_4$ –HSAC used. Then, to identify the correlation coefficient ( $R^2$ ), the isotherm and kinetic models were assessed, taking into account the following: values of the statistical goodness-of-fit parameters of the sum of square errors ( $SSE$ ), Chi-square test ( $\chi^2$ ), hybrid fractional error functions ( $H\text{YBIRD}$ ), and Marquardt's percent standard deviation ( $M\text{PSD}$ ), as shown by Eqs. (3–6) [29–31].

$$\text{Sum of squared errors (SSE)} = \sum_{i=1}^n (q_{\text{exp}} - q_{\text{ecal}})^2 \quad (3)$$

$$\text{Chi - square test } (\chi^2) = \sum_{i=1}^n \left[ \frac{(q_{\text{exp}} - q_{\text{ecal}})^2}{q_{\text{ecal}}} \right] \quad (4)$$

$$\text{Hybrid fractional error functions (HYBIRD)} = \sum_{i=1}^n \left[ \frac{(q_{\text{exp}} - q_{\text{ecal}})^2}{q_{\text{ecal}}} \right]_i \quad (5)$$

$$\text{Marquardt's percent standard deviation (MPSD)} = \sum_{i=1}^n \left[ \frac{q_{\text{exp}} - q_{\text{ecal}}}{q_{\text{ecal}}} \right]^2 \quad (6)$$

where  $q_{\text{exp}}$  and  $q_{\text{ecal}}$  represent the experimental and calculated uptakes determined, respectively, from Eq. (1) and the application of the theoretical model with the experimental data.

### 3 Results and discussion

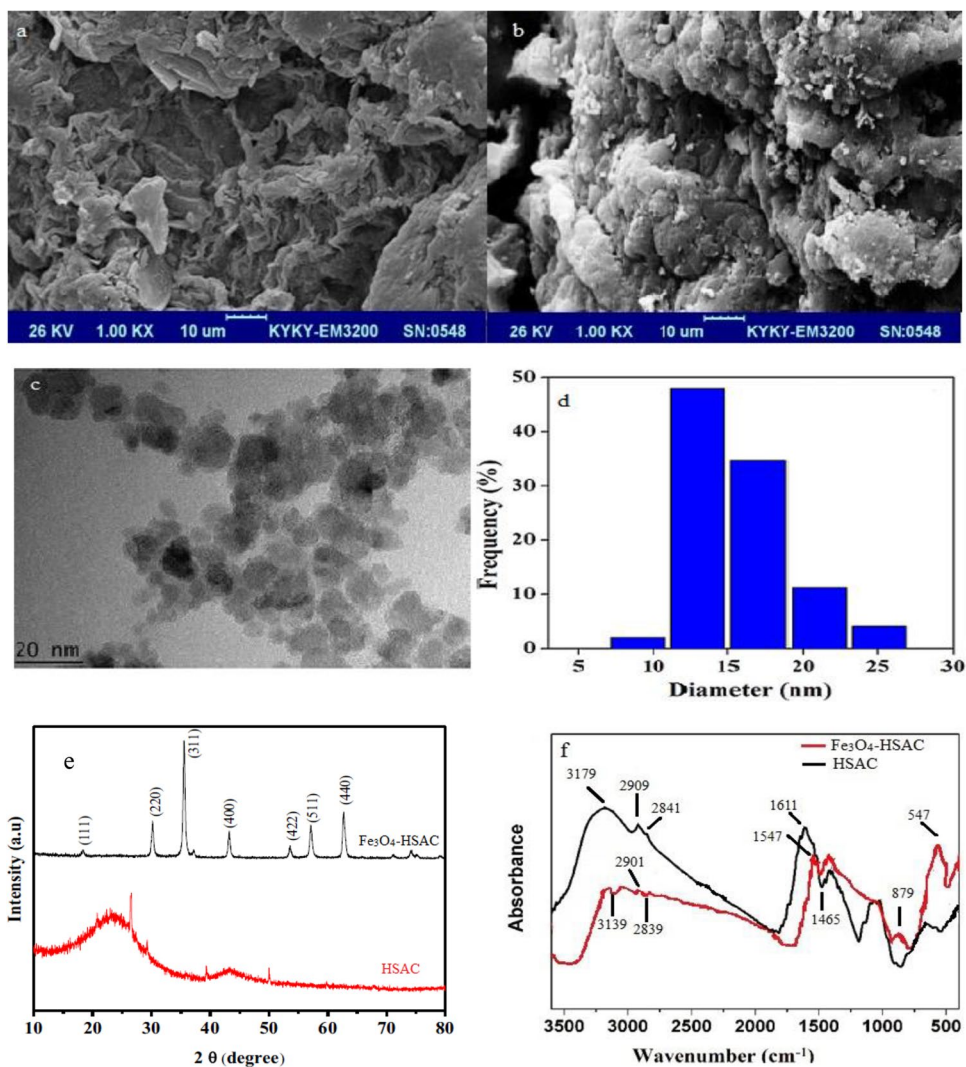
#### 3.1 Morphological and structural characterization

The SEM analysis of the  $\text{Fe}_3\text{O}_4$ –HSAC, prior to and post-fluoride ion adsorption, is revealed in Fig. 1a–b. In Fig. 1a, the adsorbent, with its variety of pore sizes, and disorganized structural pattern, is shown depicting the morphology of an undisturbed hazel shell. From Fig. 1b, a considerable transformation is evident from a morphological matrix to spongy porous texture, due to the iron oxide impregnated within the carbon structure [32]. This implies the creation of iron oxide particles dispersed sufficiently well to cover the HSAC. Furthermore, post-adsorption, the fluoride ions fill these adsorbent pores, as shown in Fig. 1b.

The synthesized  $\text{Fe}_3\text{O}_4$ –HSAC was analyzed in terms of size and morphology using TEM. From the  $\text{Fe}_3\text{O}_4$ –HSAC image (Fig. 1c), it was clear that most nanoparticles have a spherical shape. From the image, most of the particles appeared “rounded cubic” in shape and clumped together, possibly caused by the  $\text{Fe}_3\text{O}_4$ –HSAC magnetic properties. A histogram showing particle size distribution was plotted (Fig. 1d) with 13.1 nm particle size on average and 14.8 nm standard deviation. According to the XRD analysis, the synthesized  $\text{Fe}_3\text{O}_4$ –HSAC showed a crystallite size of 12.7 nm as will be illustrated later, which concurred with the findings of the TEM, revealing size distribution between 11.0 and 15.0 nm.

Examination of the crystal structure and phase purity of the synthesized  $\text{Fe}_3\text{O}_4$ –HSAC nanoparticles was also contemplated. From Fig. 1e, the typical XRD pattern of the HSAC and  $\text{Fe}_3\text{O}_4$ –HSAC samples is evident. It can be seen from the HSAC XRD that the activated carbon pattern showed an amorphous halo centered at  $2\theta = 23^\circ$ , which refers to the reflection of the plane (002), a common feature of non-crystalline structures such as activated carbon. In the XRD pattern, the stronger peaks imply high purity and good crystalline structure, while the broadening of the peak represents the creation of the  $\text{Fe}_3\text{O}_4$ –HSAC nanoparticles [18]. In the  $\text{Fe}_3\text{O}_4$ –HSAC XRD spectrum, six main crystallization peaks at  $2\theta = 30.08, 35.50, 43.15, 53.38, 57.07,$  and  $62.81^\circ$  were detected, corresponding to the 220, 311, 400, 422, 511, and 440 diffraction planes. The XRD peak seen at  $2\theta = 35.50^\circ$  was produced by the  $\text{Fe}_3\text{O}_4$  incorporation, while the peaks  $2\theta = 30.08^\circ$  and  $43.15^\circ$  were caused by the joint contribution of the  $\text{Fe}_3\text{O}_4$  and HSAC [33]. The

**Fig. 1** SEM images of  $\text{Fe}_3\text{O}_4$ -HSAC before (a) and after adsorption (b), TEM images of  $\text{Fe}_3\text{O}_4$ -HSAC (c), particle size distribution histogram (d), XRD patterns of HSAC and  $\text{Fe}_3\text{O}_4$ -HSAC (e), FTIR spectra (f)



appearance of these well crystallized phases in the XRD analysis is related to the combined effect of magnetizer  $\text{F}_3\text{O}_4$  and graphite structure from the activated carbon diffractions. This fact is also confirmed by the complete crystallography transformation of hazelnut shell structure which has an amorphous crystallinity [34]. Thus, the results of the XRD analysis for  $\text{Fe}_3\text{O}_4$ -HSAC confirm that  $\text{Fe}_3\text{O}_4$  nanoparticles have been successfully incorporated into HSAC. For the crystal structure of the prepared nanocomposite, the face-centered cubic with lattice constant  $a = 8.4272 \text{ \AA}$  was identified, which suitably corresponded to the JCPDS (89–3854) data ( $a = 8.393 \text{ \AA}$ ). The Scherrer formula, cited below, was applied to determine the average crystallite size of the  $\text{Fe}_3\text{O}_4$ -HSAC samples [35]. Based on this formula, the average crystallite size of  $\text{Fe}_3\text{O}_4$ -HSAC nanocomposite was 12.7 nm.

$$D = 0.9\lambda / \beta \cos\theta \quad (7)$$

where  $D$  (nm) indicates the average crystallite size,  $\beta$  (radians) refers to the half maximal peak width identified at any  $2\theta$  (radians) in the XRD pattern, and  $\lambda$  (0.1540 nm) represents the wavelength of the applied X-ray.

The FTIR spectra, shown in Fig. 1f, display several functional groups present on the HSAC and  $\text{Fe}_3\text{O}_4$ -HSAC surfaces. In the case of the FTIR spectrum of the HSAC sample, a broad absorption band is visible at about  $3179 \text{ cm}^{-1}$ ; this corresponds to the O–H stretching vibration of the hydroxyl functional groups arising from hemicellulose, cellulose, lignin, and other polymeric compounds [36]. At bands 2909, 2841, and  $14,265 \text{ cm}^{-1}$ , small peaks were observed, related to the C–H stretching vibrations (both symmetric and asymmetric) [20]. Further, the band identified at  $1611 \text{ cm}^{-1}$  reflects the C=O stretching vibrations of the carboxylate group [37]. These functional groups represent a partial carbonization of hazelnut shell, which implies that the end product of  $\text{F}_3\text{O}_4$  and hazel shell were not fully carbonated. Further, on examining the FTIR spectrum of

the  $\text{Fe}_3\text{O}_4$ -HSAC, a shift was detected in the HSAC band at 1611 to 1547  $\text{cm}^{-1}$ ; this shift is caused by the ferric carboxylate produced in response to doping with the  $\text{Fe}_3\text{O}_4$  [19]. The other groups observed in the FTIR spectrum, which were allocated to the bands at 3139  $\text{cm}^{-1}$  (O–H stretching vibration), 2901, 2839  $\text{cm}^{-1}$  (C–H stretching vibrations), 1547  $\text{cm}^{-1}$  (C=O stretching), and 1465  $\text{cm}^{-1}$  (C–H stretching), and the vibration of the functional group of –CO, –OH, and CH at 879  $\text{cm}^{-1}$  (aromatic C–H bending) clearly indicated the presence of the HSAC. Also, a new intensive peak visible at 547  $\text{cm}^{-1}$  reveals the Fe–O stretching mode of the layer of  $\text{Fe}_3\text{O}_4$ .

The sample was examined and its porous structure was evaluated using the  $\text{N}_2$  adsorption–desorption analysis. In Fig. 2a–b, the  $\text{N}_2$  adsorption and desorption isotherms and distribution of pore size are displayed. From the BET test, the specific surface area of  $\text{Fe}_3\text{O}_4$ -HSAC is around 624.4

$\text{m}^2/\text{g}$ , which is below the HSAC (685.6  $\text{m}^2/\text{g}$ ), and can be possibly caused by the overlapping of the active adsorbent sites by  $\text{Fe}_3\text{O}_4$ .

As depicted in Fig. 2a, the characteristic-type IV hysteresis loop is observed in the P/P<sub>0</sub> range from 0.6 to 1.0, implying a mesoporous structure present in the samples. The distribution of pore size, as evident from Fig. 2a–b, was calculated using BJH. This suggests that the sharp peaks for the HSAC and  $\text{Fe}_3\text{O}_4$ -HSAC, respectively, are present at 9.5 nm and 13.2 nm. Other peaks are also seen, for both the adsorbents, revealing several mesopores in the samples, strongly concurring with the SEM results. The rich internal mesoporous structure can raise the contact surface between the adsorbent and adsorbate, resulting in adequate numbers of active sites available for the adsorbent–ion reactions.

The results for the properties of the  $\text{Fe}_3\text{O}_4$ -HSAC and HSAC are listed in Table 1, namely moisture, total pore

**Fig. 2**  $\text{N}_2$  adsorption–desorption isotherms; inset: pore size distributions from the adsorption branches using the BJH method (a–b) and magnetic hysteresis loops (c)

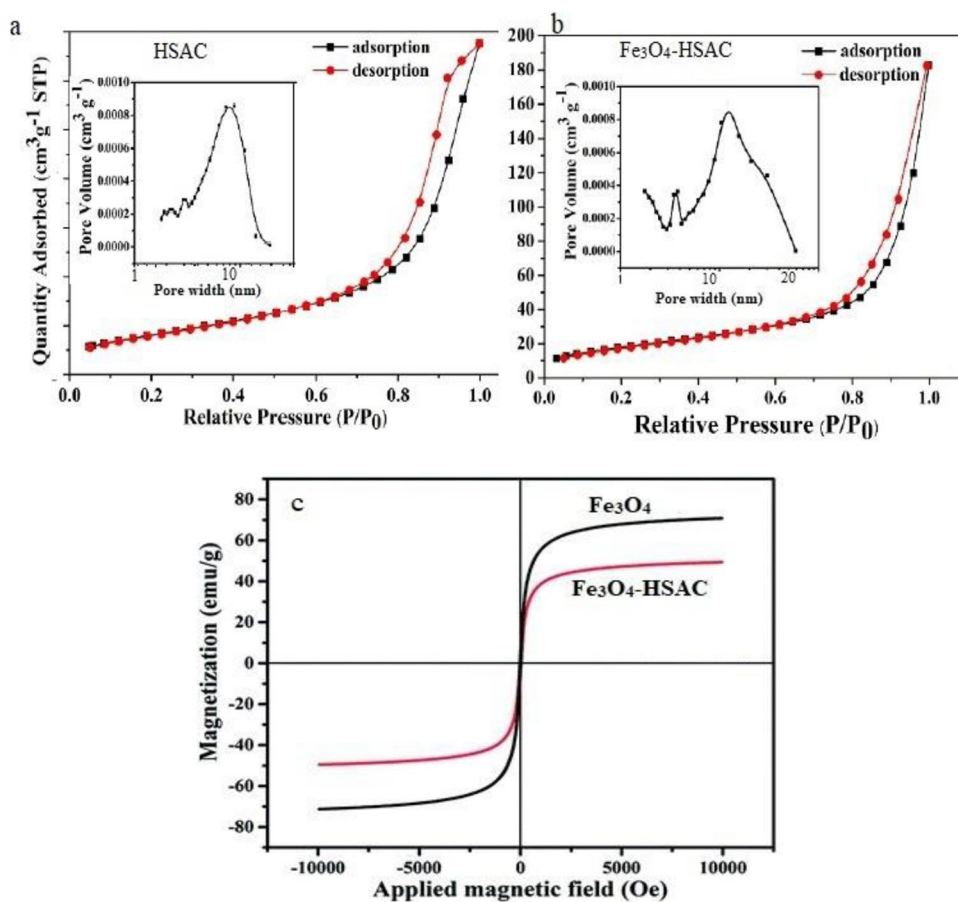


**Table 1** Characteristics of the  $\text{Fe}_3\text{O}_4$ -HSAC and HSAC

Material	Moisture %	Pore volume ( $\text{cm}^3/\text{g}$ )	Average pore diameter (nm)	C %	H %	Fe %	N %	O %
$\text{Fe}_3\text{O}_4$ -HSAC	0.14	0.612	15.2	42.2	3.2	9.9	1.1	43.2
HSAC	0.1	0.604	11.6	47.8	3.95	0.41	1.18	46.4

volume, and the quantities of the different elements such as carbon, nitrogen, iron, oxygen, and hydrogen. As evident, in HSAC the percentage of iron was very low; however, in the  $\text{Fe}_3\text{O}_4$ -HSAC synthesized, the iron percentage achieves 9.9%, an indicator of the iron entering into the intended composition.

With the aid of the VSM physical property measurement system, the magnetic characterizations of the  $\text{Fe}_3\text{O}_4$  NPs and  $\text{Fe}_3\text{O}_4$ -HSAC were tested at ambient temperature. This study was performed by assessing the effect of the saturation magnetization ( $M_s$ ) and coercive field ( $H_c$ ) by employing a magnetic field in the  $-10,000$  to  $10,000$  Oe range. As each of the particles can act as a thermally agitated permanent magnet, the  $\text{Fe}_3\text{O}_4$  NPs normally display superparamagnetic behavior. Materials like these usually represent the hysteresis loops ( $M$ - $H$  curves). The  $M_s$  values of the  $\text{Fe}_3\text{O}_4$  NPs and  $\text{Fe}_3\text{O}_4$ -HSAC were identified as 70.85 and 49.36 emu/g, respectively (Fig. 2c). The exaggerated hysteresis loops present, more strongly confirm their superparamagnetic property; however, lowering the saturation magnetization of the  $\text{Fe}_3\text{O}_4$ -HSAC indicates a weakening of the magnetic power of the nanoparticles caused by the HSAC grafting on the particle surface.

The experiment on magnetic separation promoted the  $\text{Fe}_3\text{O}_4$ -HSAC dispersion through shaking or ultrasonication, in order to produce a stable suspension, avoiding either settlement or aggregation within 48 h. Through the application of a magnetic field, the particles can be rapidly separated from the solution, and the particles thus collected were once again dispersed into the solution after the magnetic field was removed; the noteworthy events included the approval of the outstanding magnetic responsivity and the characteristic dispersibility of the  $\text{Fe}_3\text{O}_4$ -HSAC.

## 3.2 Study of the effects

### 3.2.1 Adsorption time and initial fluoride concentration

At different fluoride concentrations (25–100 mg/L), as shown in Fig. 3, the removal efficiency of fluoride by  $\text{Fe}_3\text{O}_4$ -HSAC was plotted in relation to the adsorption time (10–150 min). The importance of this experiment was the identification of the equilibrium time at which the highest possible adsorption was accomplished. As is evident, the first half-hour of the adsorption time was when the highest removal occurred; however, after 75 min, the adsorption efficiency achieved full equilibrium status. As the contact time increased, the contact between the fluoride ions and the  $\text{Fe}_3\text{O}_4$ -HSAC also increased, causing the rise in the adsorption rate, which is more evident in the first few minutes; however, as the contact time increased, the adsorption rate decreased. This may have been caused by a reduction in the concentration of the soluble fluoride and a lower number of

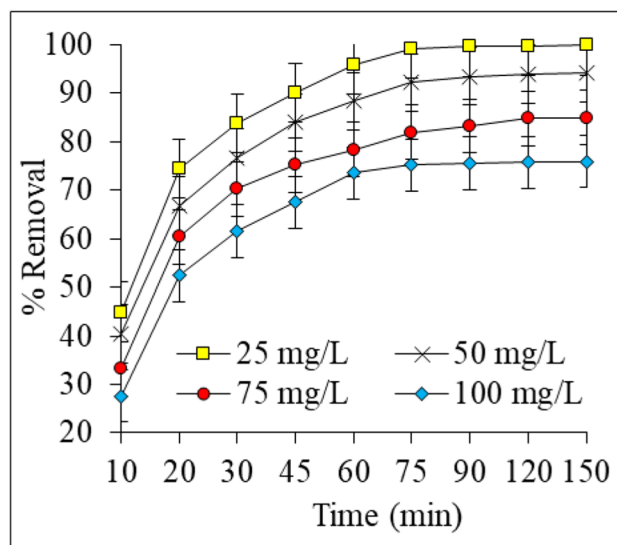


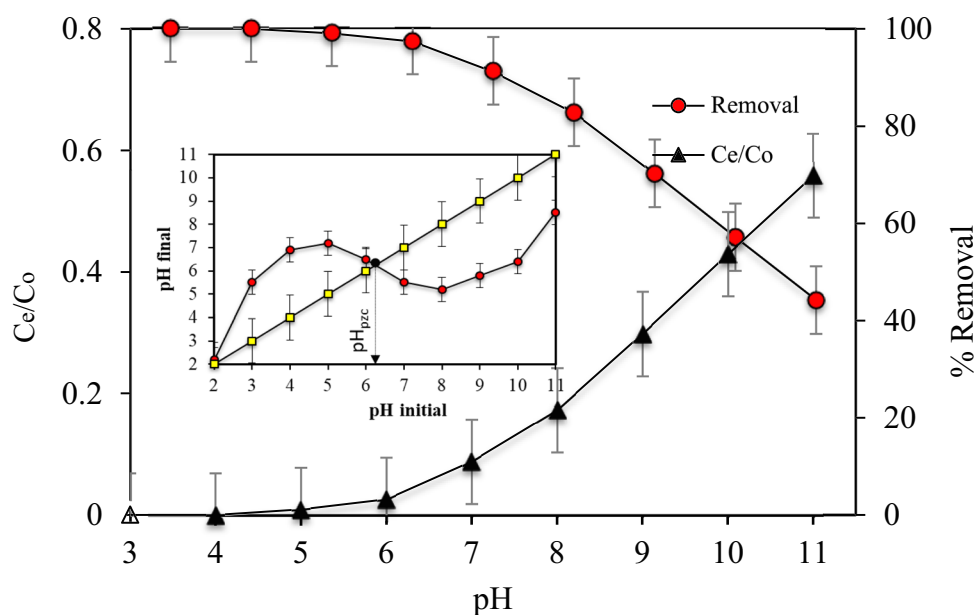
**Fig. 3** The removal efficiency of fluoride by  $\text{Fe}_3\text{O}_4$ -HSAC at different times of adsorption and concentrations of pollutant

sites present on the  $\text{Fe}_3\text{O}_4$ -HSAC surface for active adsorption because during the early phases of the adsorption, several vacant sites were available. However, over time, the fluoride ions occupied these sites [38, 39]. Almost at the exact same time as the results of the effect exerted by the adsorption time, Fig. 3 shows the outcomes of the fluoride removal efficiency and the  $\text{Fe}_3\text{O}_4$ -HSAC removal efficiency as a function of the initial concentration of the fluoride (25, 50, 75, and 100 mg/L). Obviously, when the fluoride concentrations were low, the removal rate escalated, even exceeding the rate noted at high concentrations. This phenomenon occurs because the adsorbent used possesses limited number of adsorption sites which, as the pollutant concentration rises, speeds up their saturation capacity, and thus induces a reduction in the removal efficiency. The results given from Fig. 3 show good correspondence with the results reported in earlier works [40, 41].

### 3.2.2 pH and $\text{pH}_{\text{pzc}}$ values

From Fig. 4, the results of the effects of the pH value on the fluoride adsorption using  $\text{Fe}_3\text{O}_4$ -HSAC are given. In fact, the charge on the adsorbent surface is an important factor that ascertains the electrostatic interaction between the surface of adsorbent and adsorbate (pollutant) molecules which, in turn, affects the adsorption. The  $\text{Fe}_3\text{O}_4$ -HSAC surface charge is dependent upon the chemical and electronic properties of the functional groups present on its surface, as well as upon the pH of the solution, during the actual adsorption [42]. The pH value, at which the negative and positive concentrations of the surface become equal (meaning the surface

**Fig. 4** Effect of pH values on fluoride removal using  $\text{Fe}_3\text{O}_4$ -HSAC and  $\text{pH}_{\text{pzc}}$  analysis



is electrically neutral), is termed the  $\text{pH}_{\text{pzc}}$  parameter. When the pH values drop to below the  $\text{pH}_{\text{pzc}}$ , the  $\text{Fe}_3\text{O}_4$ -HSAC surface carries a positive charge, favoring the anion adsorption. On the contrary, when the pH values are higher than the  $\text{pH}_{\text{pzc}}$ , the  $\text{Fe}_3\text{O}_4$ -HSAC surface carries a negative charge [43], supporting the cation adsorption. From the results displayed in Fig. 4, the  $\text{pH}_{\text{pzc}}$  for  $\text{Fe}_3\text{O}_4$ -HSAC is 6.2, which shows that when the pH of the solution drops to less than 6.2, the fluoride ion adsorption onto the  $\text{Fe}_3\text{O}_4$ -HSAC composite is enhanced. In this study, for a concentration of 25 mg/L and an adsorbent dose of 0.75 g/L, at temperature of 25 °C and duration of 75 min, the pH tests were conducted in the range from 3 to 11. According to the results revealed in Fig. 4, the removal percentage shows a rapid reduction from 99.1 to 44.2% in response to the pH rising from 3 to 11. As cited earlier, the  $\text{pH}_{\text{pzc}}$  for  $\text{Fe}_3\text{O}_4$ -HSAC was around 6.2. Therefore, at  $\text{pH} > 6.2$ , the adsorbent surface carried a negative charge and hindered the transport of the fluoride anions ( $\text{F}^-$ ) from gaining access to the binding sites on the  $\text{Fe}_3\text{O}_4$ -HSAC caused by electrostatic repulsion. Besides, when the pH is high, fairly high concentrations of the  $\text{OH}^-$  strongly contend with the fluoride ions for adsorption onto the active sites on the surface of the  $\text{Fe}_3\text{O}_4$ -HSAC, resulting in lowering the adsorption capacity. At  $\text{pH} < 6.2$ , a significant rise in the adsorption was observed, induced by the intensive fluoride anion adsorption, carrying a negative surface charge of  $\text{Fe}_3\text{O}_4$ -HSAC [44]. In the pH between 3 and 5, a small difference was observed in the adsorption. Therefore, in the rest of this study, pH 5 was chosen for easier adjustment during the experiments.

### 3.2.3 $\text{Fe}_3\text{O}_4$ -HSAC dose

In the adsorption experiments, one of the crucial parameters that help to establish the quantity of the adsorbent required to power the adsorption process is the optimal adsorbent dose. The optimal dose of  $\text{Fe}_3\text{O}_4$ -HSAC was estimated using the batch adsorption experiments, through mixing a variety of adsorbents in the 0.1 to 1 g range using 50 ml of the 25 mg/L fluoride solution, maintaining the pH at 5, temperature at 25 °C, in contact time of 75 min. From Fig. 5, the  $\text{Fe}_3\text{O}_4$ -HSAC adsorption capacity is observed to reduce in all the dose ranges; in the initial stage, the removal efficiency escalates rapidly after which it achieves equilibrium at 0.75 g/L a dose. This may occur probably because when high doses of adsorbent are present, the adsorption sites show either overlap or accumulation, which decrease their contact with the fluoride ions [45]. The optimal dose of the adsorbent selected in this study was 0.75 g/L, as this was the minimum  $\text{Fe}_3\text{O}_4$ -HSAC dose, at which the removal as well as the adsorption efficiency was high.

### 3.2.4 Adsorption at different temperatures and thermodynamic study

The experiments performed to investigate the effect of temperature on the uptake of fluoride onto the surface of the  $\text{Fe}_3\text{O}_4$ -HSAC adsorbent were done at 15, 25, 35, and 45 °C under the conditions cited:  $\text{pH} = 5$ , initial concentration 100 mg/L, and quantity of adsorbent = 0.75 g/L. In Fig. 6, the experimental findings are listed. The adsorption capacity is observed to rise from 89.2 to 125.6 mg/g with the equilibrium time of 75 min;



**Fig. 5** The adsorption behavior for the fluoride at different Fe<sub>3</sub>O<sub>4</sub>-HSAC doses

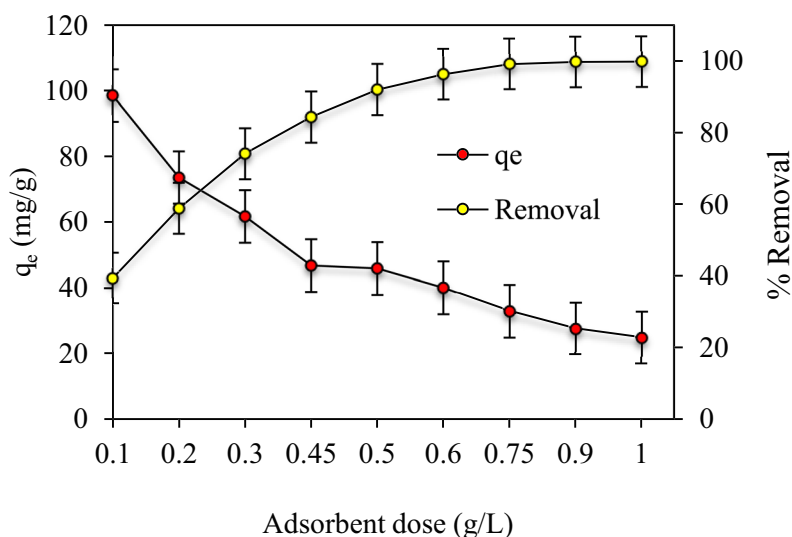
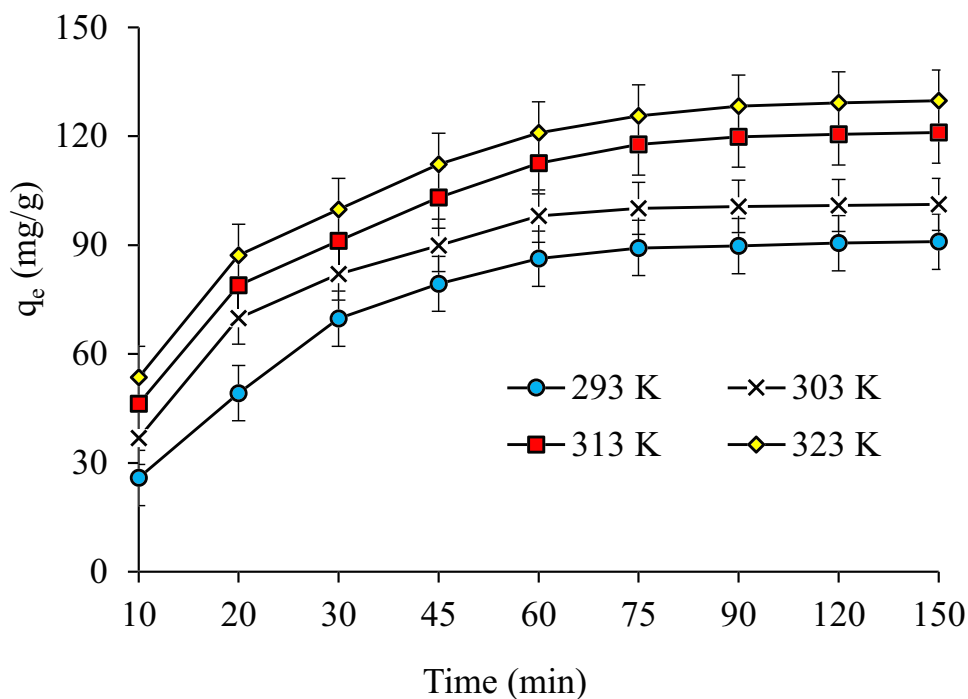


**Fig. 6** Effect of temperature on the Fe<sub>3</sub>O<sub>4</sub>-HSAC adsorption capacity for fluoride



the rise in temperature from 15 to 45° C suggests that the adsorption of the fluoride onto the Fe<sub>3</sub>O<sub>4</sub>-HSAC was more advantageous when the temperature was high. This heightened adsorption capacity of the Fe<sub>3</sub>O<sub>4</sub>-HSAC for fluoride in response to temperature may be linked to the improved mobility of the fluoride ions present in the solution [46]. Further, any increase in the temperature boosts the fluoride diffusion rate across the external boundary layer and internal pores of the Fe<sub>3</sub>O<sub>4</sub>-HSAC particles because the viscous forces in the aqueous phase are less resistant [27].

In thermodynamic studies, the Gibbs free energy change ( $\Delta G^\circ$ ), enthalpy change ( $\Delta H^\circ$ ), and entropy change ( $\Delta S^\circ$ ), which are the thermodynamic parameters, were determined to assess the thermodynamic feasibility and spontaneity of the process under investigation. The thermodynamic parameters were calculated, using the variations in the thermodynamic distribution coefficient  $K_d$  with temperature change, according to the equation [47]:

$$K_d = q_e/C_e \tag{8}$$

The equation given below is applied to calculate the  $\Delta H^\circ$  and  $\Delta S^\circ$  [48]:

$$\ln(K_d) = \frac{\Delta S^\circ}{R} - \frac{\Delta H^\circ}{RT} \quad (9)$$

The slope and the intercept of the straight line achieved by plotting the  $\ln(K_d)$  vs.  $1/T$  to produce it are employed to estimate the values of  $\Delta H^\circ$  and  $\Delta S^\circ$ , respectively, as revealed in Table 2. The  $\Delta H^\circ$  value obtained was 56.01 kJ/mol, whereas the  $\Delta S^\circ$  value was 0.198 kJ/mol. The positive value acquired for the  $\Delta H^\circ$  may be indicative of the endothermic and physical nature of the fluoride ion adsorption by the  $\text{Fe}_3\text{O}_4$ -ACLM. Further, the positive  $\Delta S^\circ$  value suggested that a rise in the degree of freedom was identifiable at the solid–liquid interface, which caused the fluoride ions to be immobilized onto the surface of the  $\text{Fe}_3\text{O}_4$ -ACLM nanocomposite.

The equation given in the following was applied to calculate  $\Delta G^\circ$  [49]:

$$\Delta G^\circ = \Delta H^\circ - T\Delta S^\circ \quad (10)$$

The free energy change ( $\Delta G^\circ$ ) was found to have a negative value, which represents a product-favoring spontaneous reaction. As observed, a rise in the temperature resulted in more negative values for the  $\Delta G^\circ$ , providing proof that the spontaneity levels of the reaction rise correspond to the increase in temperature. The higher temperatures appeared more favorable for the fluoride adsorption onto the  $\text{Fe}_3\text{O}_4$ -ACLM adsorbent [50, 51]

### 3.3 Adsorption isotherms

The models for statistical error validity were contemplated for both isotherm and kinetics data. A good understanding of the fluoride solution– $\text{Fe}_3\text{O}_4$ -HSAC adsorbent interaction is reached by examining the isotherm models. Six types of isotherms were used in this study, the equations of which are shown in Table 3 [52, 53]. They are the Freundlich, Temkin, D–R, Halsey, Jovanovich, and Langmuir models. Using the high regression coefficient and lower error coefficient, a better fit with the equilibrium data could be determined, as displayed in Table 3. In the case of the Halsey and

Freundlich isotherms, the regression coefficient exceeds 0.99 and reveals a lower error coefficient than the other isotherms, both of which explain the properties of adsorption for heterogeneous surfaces.

It is recognized that  $K_F$  (adsorption capacity based on Freundlich model) and  $n_F$  (adsorption intensity) represent the typical parameters of the Freundlich model. These two parameters are determined depending upon the straight line acquired from plotting  $\log Q_e$  against  $\log C_e$ . In addition, the surface heterogeneity and favorability of the fluoride adsorption onto the  $\text{Fe}_3\text{O}_4$ -HSAC are determined by parameter  $1/n_F$ . When values exceeding unity are identified for  $1/n_F$ , cooperative adsorption can be confirmed, as determined in this study ( $1/n_F = 3.82$ ).

For Langmuir model, from the slope and intercept of the linear plot of  $C_e/Q_e$  vs  $1/C_e$ , the  $K_L$  and  $Q_{\max}$  were determined. In addition, the dimensionless and separation Langmuir factor ( $R_L$ ) is recognized as useful in establishing whether the adsorption process of the fluoride onto the  $\text{Fe}_3\text{O}_4$ -HSAC was conducive; in other words, it explains the favorability or otherwise of the character of the adsorption; therefore, according to this definition, adsorption is unfavorable when  $R_L > 1$ ; it is linear when  $R_L = 1$ ; it is favorable when  $0 < R_L < 1$ ; and it is irreversible when  $R_L = 0$  [43]. In the present study, the  $R_L$  value was found to be 0.192, which is below one, and therefore typical for favorable adsorption. The mechanism of the fluoride and  $\text{Fe}_3\text{O}_4$ -HSAC system having a Gaussian energy distribution onto a heterogeneous surface is usually determined by D–R. The parameters of this model, i.e.,  $Q_m$  and  $B$ , were determined from intercept and slope of linear plot of  $\ln q_e$  vs  $\epsilon^2$ . Further, in the D–R model, the mean energy ( $E$ ) drops below 8 kJ/mol, which drives the main physisorption of fluoride [54].

Further, Table 4 gives the comparison of the maximum adsorption capacity derived from the Langmuir isotherm with that of the other adsorbents, for the elimination of fluoride, and as is evident, the adsorption capacity of this adsorbent is greater than that of the other adsorbents for fluoride removal. In addition, the  $\text{Fe}_3\text{O}_4$ -HSAC adsorption capacity was higher than that for HSAC, indicative of the role of the  $\text{Fe}_3\text{O}_4$  in the enhancement of adsorption capacity of HSAC.

### 3.4 Adsorption kinetics study

The rate of adsorption kinetics was estimated to assess the binding rate of the fluoride onto the  $\text{Fe}_3\text{O}_4$ -HSAC and to explain the mechanism involved in the process of sorption. The pseudo-first order (PFO), pseudo-second order (PSO), Elovich, and fractional power equation were some of the kinetics models employed for different concentrations (25–100 mg/L). Besides, liquid film diffusion (LFD) and intraparticle diffusion (IPD) models were used to model the experimental data to examine the part that the IPD rate played in adsorption control [60–62]. From the results of these studies, as shown in Table 5, it becomes

**Table 2** Thermodynamic parameters for fluoride adsorption onto the  $\text{Fe}_3\text{O}_4$ -HSAC

T (K)	$\Delta G^\circ$ (kJ/mol)	$\Delta H^\circ$ (kJ/mol)	$\Delta S^\circ$ (kJ/mol K)
288	−2.37	56.01	0.198
298	−3.44		
308	−5.88		
318	−8.11		

**Table 3** The isotherm parameters of fluoride adsorption onto the Fe<sub>3</sub>O<sub>4</sub>–HSAC adsorbent

Models	Parameters
<p><b>Langmuir</b>  <math>\frac{1}{Q_e} = \frac{1}{Q_{max}} + \frac{1}{Q_{max}K_L C_e}</math>, <math>R_L = \frac{1}{1+K_L C_e}</math>                      K<sub>L</sub> = Langmuir isotherm constant (L/mg)                      Q<sub>max</sub> = maximum monolayer coverage–adsorption capacity (mg/g)</p>	<p>Q<sub>max</sub> 146.2                      K<sub>L</sub> 0.042                      R<sup>2</sup> 0.927                      R<sub>L</sub> 0.192                      HYBRID 8.34                      MPSD 11.6                      SSE 6.95                      X<sup>2</sup> 4.32</p>
<p><b>Freundlich</b>  <math>\log Q_e = \log K_F + \frac{1}{n_F} \log C_e</math>                      Q<sub>e</sub> = quantity of fluoride adsorbed/g adsorbent (mg/g). K<sub>F</sub> = Freundlich indicator of adsorption capacity. n<sub>F</sub> = adsorption intensity parameter</p>	<p>K<sub>F</sub> 2.45                      1/n<sub>F</sub> 3.82                      R<sup>2</sup> 0.992                      HYBRID 2.76                      MPSD 3.75                      SSE 1.94                      X<sup>2</sup> 2.79</p>
<p><b>Temkin</b>  <math>Q_e = \frac{RT}{b_T} \ln A_T + \frac{RT}{b_T} \ln C_e</math>                      b<sub>T</sub> = Temkin isotherm constant related to the heat of adsorption. A<sub>T</sub> = Temkin isotherm equilibrium binding constant (L/g).                      R = universal gas constant (8.314 J/mol/K)                      T = absolute temperature in Kelvin. B = RT/b<sub>T</sub> = constant related to heat of sorption (J/mol) obtained from either intercept or slope</p>	<p>b<sub>T</sub> 8.29                      A<sub>T</sub> 0.726                      R<sup>2</sup> 0.879                      B 298.8                      HYBRID 9.25                      MPSD 12.4                      SSE 9.86                      X<sup>2</sup> 9.4</p>
<p><b>D-R</b>  <math>\ln q_e = \ln q_m - B \epsilon^2</math>, <math>E = \frac{1}{2B^{0.5}}</math>  <math>\epsilon = RT \ln \left[ 1 + \frac{1}{C_e} \right]</math>                      Q<sub>m</sub> = theoretical adsorption isotherm saturation capacity (mg/g). B refers to the D–R isotherm constant (mol<sup>2</sup>/kJ<sup>2</sup>). ε is Polanyi potential</p>	<p>Q<sub>m</sub> 95.4                      R<sup>2</sup> 0.889                      E 4.59                      HYBRID 11.2                      MPSD 9.8                      SSE 12.2                      X<sup>2</sup> 8.76</p>
<p><b>Halsey</b>  <math>\log Q_e = \left[ \left( \frac{1}{n_H} \right) \ln K_H \right] - \left( \frac{1}{n_H} \right) \ln C_e</math>                      K<sub>H</sub> = Halsey isotherm constant. n<sub>H</sub> is the Halsey isotherm exponent</p>	<p>K<sub>H</sub> 4.73                      n<sub>H</sub> 0.457                      R<sup>2</sup> 0.995                      HYBRID 7.76                      MPSD 4.54                      SSE 3.91                      X<sup>2</sup> 3.25</p>
<p><b>Jovanovic</b>  <math>\ln Q_e = \ln Q_m - K_J C_e</math>                      K<sub>J</sub> = Jovanovic isotherm constant (L/g)</p>	<p>Q<sub>m</sub> 76.4                      K<sub>J</sub> 0.381                      R<sup>2</sup> 0.849                      HYBRID 4.52                      MPSD 8.47                      SSE 9.72                      X<sup>2</sup> 7.78</p>

evident that from all the kinetic models examined, the highest correlation coefficient (R<sup>2</sup>) was found to be related to PSO (> 0.99).

Statistical error functions have also been used to endorse the kinetic models, which were also more suited for the pseudo-second-order kinetics than the others. The PSO

**Table 4** Comparison of adsorption capacities reported for various adsorbents for fluoride

Adsorbent	$Q_{\max}$ (mg/g)	Reference	Adsorbent	$Q_{\max}$ (mg/g)	Reference
Neem leaf powder	34.6	[30]	Activated Alumina	52.3	[22]
Sorghum	36.8	[14]	Zeolite	56.2	[14]
Eucalyptus-AC	38.7	[17]	Eggshell powder	56.4	[55]
Bone Char	39.2	[56]	MgO nano-particles	64.1	[31]
Azolla	41.9	[57]	Nano-alumina	65.1	[8]
Chitosan	43.1	[58]	MWCNT	71.2	[7]
Brushite	45.2	[59]	Granular ceramic	73.2	[10]
Lemna minor	51.3	[1]	Fe <sub>3</sub> O <sub>4</sub> -HSAC	146.2	This study

**Table 5** Kinetic parameters for fluoride adsorption on Fe<sub>3</sub>O<sub>4</sub>-HSAC

Model	Parameters	25 mg/L	50 mg/L	75 mg/L	100 mg/L
Experimental $Q_e$	—	33.2	62.8	84.9	101.2
PFO	$q_e$ (cal)	12.7	34.9	53.4	75.3
$\text{Log}(q_e - q_t) = \log q_e - \frac{K_1}{2.303} t$	$K_1$	0.032	0.039	0.034	0.045
$q_e$ = adsorption capacity at equilibrium time,	$R^2$	0.912	0.927	0.931	0.872
$q_t$ = adsorption capacity at time $t$ (mg/g),	$X^2$	11.2	9.72	9.23	8.24
$K_1$ (1/min) = equilibrium rate constant for PFO	HYBRID	9.88	11.2	11.2	11.3
	ARE	10.4	12.7	9.82	13.4
	MPSD	12.6	14.1	12.3	7.25
PSO	$q_e$ (cal)	37.2	60.4	87.2	99.8
$\frac{t}{q_t} = \frac{1}{K_2 q_e^2} + \frac{t}{q_e}$	$K_2$	0.0037	0.0012	0.0009	0.0006
$K_2$ = equilibrium rate constant for PSO (g/mg. min)	$R^2$	0.998	0.999	0.998	0.997
	$X^2$	2.12	1.65	1.24	1.47
	HYBRID	2.19	1.42	1.51	1.64
	ARE	1.25	1.02	2.23	1.69
	MPSD	1.71	1.25	1.43	1.29
Elovich	$q_e$ (cal)	25.4	51.2	72.3	96.2
$q_t = \frac{1}{\beta} \ln(\alpha\beta) + \frac{1}{\beta} \ln(t)$	$\alpha \times 10^6$	11.9	8.42	6.24	5.17
$q_t$ = uptake at time $t$ . $\alpha$ is the initial adsorption rate (mg/g-min). $\beta$ is the desorption constant (g/mg) during any one experiment	$\beta$	0.0053	0.0035	0.0014	0.0009
	$R^2$	0.854	0.892	0.912	0.895
	$X^2$	5.12	4.72	6.89	9.15
	HYBRID	11.4	8.12	8.24	7.29
	ARE	8.43	7.15	9.43	10.6
	MPSD	7.26	11.2	8.34	9.31
Fractional Power	$q_e$ (cal)	36.9	57.4	69.8	87.2
$\log(q_t) = \log(k) + v \log(t)$	$V$	0.017	0.036	0.052	0.061
$q_t$ = uptake at time $t$ . $k$ is a constant (mg/g). $t$ is the adsorption time (min), and $v$ is a positive constant ( $< 1$ ) ( $\text{min}^{-1}$ )	$K$	27.2	35.5	43.6	53.9
	$R^2$	0.872	0.897	0.971	0.976
	$X^2$	11.4	7.24	11.2	9.24
	HYBRID	9.61	7.11	8.25	12.4
	ARE	6.24	4.24	7.13	11.3
	MPSD	8.16	8.42	7.02	8.21

appeared to be the best model as the calculated adsorption capacity ( $q_e$  (cal)) was compatible with the experimental adsorption capacity ( $q_{e\text{exp}}$ ), together with the lesser

quantities of the ASRF data noted in the SSE,  $X^2$ , HYBRID, and MSPD (Fig. 7a).

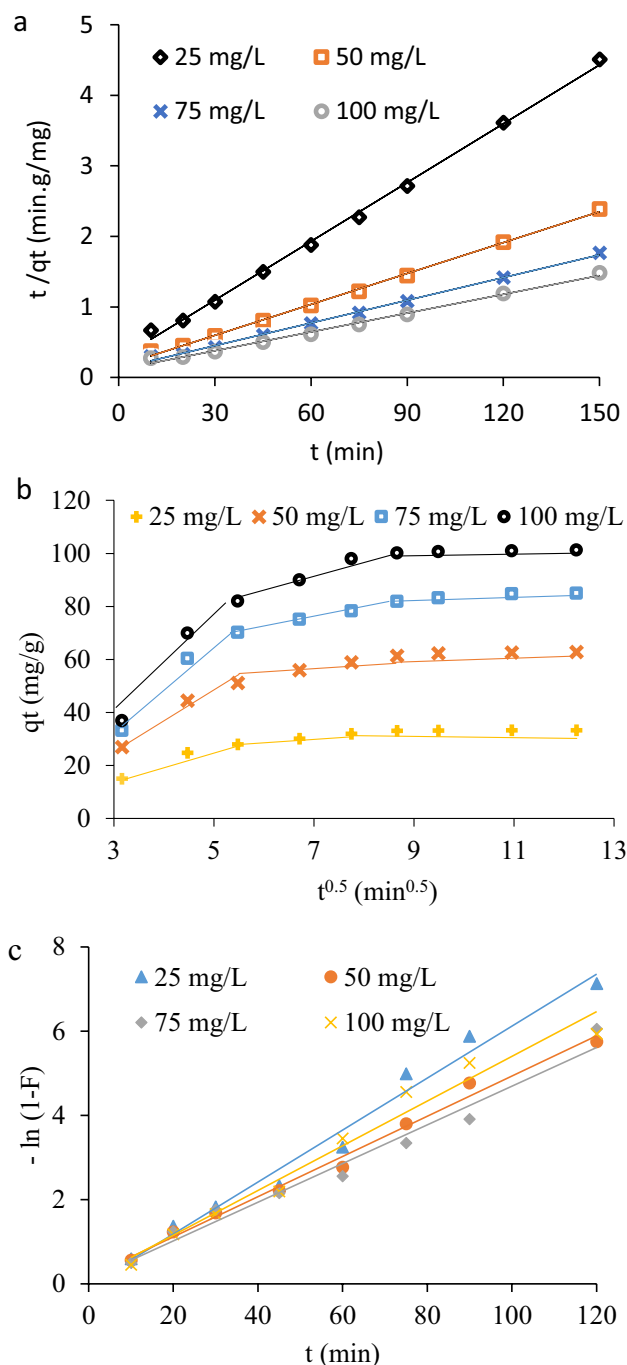


**Fig. 7** Plots presented from the analysis of pseudo-first-order (a), pseudo-second-order (b), and intraparticle diffusion (c) kinetic models

In the fractional power model, the  $v$  and  $k$  parameters are positive and rise with the increase in concentration, suggesting a speedy kinetic process. As the  $q_{eexp}$  and  $q_{ecal}$  reveal close correspondence between them, it indicates that the kinetic data have the best fit with the fractional power model. When the concentrations were low  $q_{ecal}$ , the  $R^2$  values too were low; however,

at higher concentrations better regression coefficients were acquired, implying that the adsorbents could remove the contaminant when the fluoride concentrations were at higher levels.

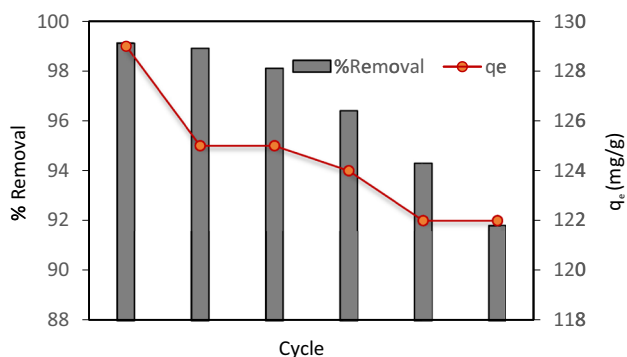
The IPD and LFD plots enabled the assessment of the mode of fluoride diffusion into the  $Fe_3O_4$ -HSAC. For both models, the coefficients are given in Table 6. For the LFD model, at all the concentrations, the regression coefficient exceeded 0.97, while for the IPD the regression coefficient involved three distinct steps with high values, as shown in Fig. 7b and c. Hence, it is clear that both the IPD and LFD models play a crucial role in adsorption kinetics. The three stages that the IPD model used reveal that the first stage has a high rate, evident in the contact time diagram up to 30 min, with a high-rate coefficient ( $K_b$ ), and over time, it gets lower in the second and third stages. As the rate coefficient is low in the third stage, this stage can for all practical intents be ignored. In the current study, during the adsorption process, the involvement of the boundary-layer diffusion was approved because the linear plots of the IPD and LFD were not pass through the origin. Therefore, neither the IPD nor the LFD is the only rate-determining step, and thus, the fluoride removal from the aqueous solution by  $Fe_3O_4$ -HSAC is jointly controlled by both the LFD and IPD [63]. Thus, the adsorbent thickness ( $C$ ) calculated using the IPD model (which exceeded 0 for all concentrations) clearly indicated that boundary-layer thickness is significant in the process of adsorption. Among the many parameters estimated in Table 6, the  $C > 0$  implies the possible involvement of the diffusion model in determining the rate controlling step.

### 3.5 Recycling process

For commercial applications, the potential of the adsorbents is assessed based on their regeneration and reuse, which have been identified as the principal parameters. The adsorption capacity of the adsorbent in this study, for the fluoride ions (25 mg/L), under the optimal conditions, cited in all the six consecutive cycles of the adsorption–regeneration process was performed, to determine the reusability of the  $Fe_3O_4$ -HSAC (Fig. 8). Depending upon the results, after six cycles, a very slight reduction was noted from 33 to 30.6 mg/g (corresponding to a decrease in the removal efficiency from 99.1 to 91.8%) for the adsorption capacity of the  $Fe_3O_4$ -HSAC for fluoride. This may be explained depending upon the loss of the active sites on the adsorbent from the sequential processes of desorption–regeneration–adsorption and the creation of a stable merger between the fluoride and active sites on the  $Fe_3O_4$ -HSAC surface [64]. However, the  $Fe_3O_4$ -HSAC revealed remarkable reusability for the fluoride removal, as only a slight drop in efficiency was detected after six adsorption–desorption cycles, with 87.67% being achieved.

**Table 6** Model parameters of fluoride adsorption onto Fe<sub>3</sub>O<sub>4</sub>-HSAC in terms of intraparticle (IPD) and liquid film diffusion (LFD)

Model	Parameters	Concentration (mg/L)			
		25	50	75	100
LFD $\ln(1 - F) = -Kt + CL$ , $F = \frac{[q_t]}{[q_e]}$ F=fractional attainment of equilibrium. K=(1/min) is the film diffusion rate coefficient	CL	0.051	0.162	0.104	0.097
	K	0.061	0.047	0.045	0.053
	R <sup>2</sup>	0.981	0.991	0.973	0.972
IPD $q_t = K_b t^{1/2} + C$ K <sub>b</sub> =IPD rate constant (mg/g. min <sup>1/2</sup> ). C=boundary-layer thickness	Stage 1				
	K <sub>b</sub>	5.68	10.9	16.2	19.8
	C	2.27	5.47	16.3	23.6
	R <sup>2</sup>	0.954	0.968	0.965	0.966
	Stage 2				
	K <sub>b</sub>	1.54	2.81	3.47	5.28
	C	19.7	37.1	51.6	55.2
	R <sup>2</sup>	0.983	0.998	0.995	0.919
	Stage 3				
	K <sub>b</sub>	0.036	0.191	0.622	0.192
	C	32.8	60.4	77.4	98.8
	R <sup>2</sup>	0.976	0.998	0.962	0.998

**Fig. 8** Reusability study of Fe<sub>3</sub>O<sub>4</sub>-HSAC on fluoride uptake (pH=5, C<sub>0</sub>=24 mg/L, temperature 25 ± 2° C, dose=0.75 g/L, and time=90 min)

## 4 Conclusion

The preparation of the Fe<sub>3</sub>O<sub>4</sub>-HSAC magnetic nanocomposite was done employing simple chemical and physical methods to remove the fluoride ions from the aqueous solutions. Using the following methods, namely SEM/EDX, BET/BJH analysis, FTIR, pH<sub>pzc</sub>, TEM, and VSM, the adsorbent properties were ascertained. The results from XRD and FTIR analysis have confirmed the microstructural/molecular transformations of hazel shell from an amorphous to a well-crystallized product, which was caused by the magnetizer F<sub>3</sub>O<sub>4</sub>. Through magnetism measurements, a strong magnetic nanocomposite was formed; the nanocomposite under study was

found to have saturation magnetization of 49.36 emu/g. The outcomes of the characterization analysis revealed that the synthesized Fe<sub>3</sub>O<sub>4</sub>-HSAC has excellent adsorptive properties such as specific surface area, functional groups, and morphology. Effect study revealed that the ability of Fe<sub>3</sub>O<sub>4</sub>-HSAC for fluoride removal was significantly dependent on the value of solution pH. Further, a thorough investigation was contemplated, on the variety of factors that affect the fluoride removal by the Fe<sub>3</sub>O<sub>4</sub>-HSAC nanocomposite. An increase in the Fe<sub>3</sub>O<sub>4</sub>-HSAC mass was found to be related to improved adsorption efficiency, with the highest removal percentage of the fluoride achieved when 0.75 g/L of the adsorbent was used. Besides, investigations performed to assess the influence exerted by the adsorption time introduced the adsorption equilibrium time as 75 min. The eligibility of the PSO kinetic model for the adsorption data was confirmed by fitting the data with the different kinetics used when performing the kinetic studies. The outcomes of the studies connected with the adsorption process indicated the part each of the different steps played, e.g., the fluoride diffusion through the boundary layer to the outer surface of the Fe<sub>3</sub>O<sub>4</sub>-HSAC nanocomposite, IPD, LFD, and fluoride adsorption via the Fe<sub>3</sub>O<sub>4</sub>-HSAC nanocomposite particles in the adsorption process under evaluation. Thermodynamic studies were also performed by assessing the various thermodynamic parameters. From the results, the fluoride removal process performed by the adsorbent in this study, i.e., the Fe<sub>3</sub>O<sub>4</sub>-HSAC nanocomposite, was physical and endothermic because a rise in the temperature of the solution was observed to be related to the improvement the adsorption capacity; the ΔH° and ΔS° values were 56.01 kJ/mol and 0.198 kJ/mol.K. Further,

negative values between  $-2.73$  and  $-8.11$  kJ/mol were identified for the  $\Delta G^\circ$ , suggesting that this process was spontaneous in nature. The  $\text{Fe}_3\text{O}_4$ -HSAC nanocomposite was utilized to removing the fluoride from the aqueous media, and the findings revealed that almost 100% removal occurred, and the nanocomposite could be re-used for six consecutive high-performance periods.

**Acknowledgements** The authors express their thankfulness to the Student Research Committee of Zahedan University of Medical Sciences for the financial support provided (code: 10629). Also, gratitude is extended for the scientific cooperation between Al-Mustaqbal University College and Zahedan University.

**Author contribution** All authors contributed to the study conception and design. Material preparation, data collection, and analysis were performed by Tariq J. Al-Musawi, Gordon McKay, and Abdullah Kadhim. The first draft of the manuscript was written by Davoud Balarak and Maryam Masoumi Joybari. All authors read and approved the final manuscript.

**Funding** This work was supported by Zahedan University of Medical Sciences, Zahedan, Iran.

## Declarations

**Conflict of interest** The authors declare no conflict of interest.

**Consent to participate** Consent has been taken from all the authors for participation in this study.

**Consent for publication** Consent has been taken from all the authors for publication of this manuscript.

## References

- Zazouli MA, Balarak D, Karimnezhad F, Khosravi F (2014) Removal of fluoride from aqueous solution by using of adsorption onto modified Lemna minor: adsorption isotherm and kinetics study. *J Mazand Uni Med Sci* 23(109):208–217
- Mohammadi AK, Yousefi M, Yaseri M, Jalilzadeh M (2017) Skeletal fluorosis in relation to drinking water in rural areas of West Azerbaijan. *Iran Scientific Reports* 17300(7):44–51
- Ma W, Ya FQ, Han M, Wang RJ (2007) Characteristics of equilibrium, kinetics studies for adsorption of fluoride on magnetic-chitosan particle. *J Hazard Mater* 143:296–302
- Bazrafshan E, Balarak D, Panahi AH, Kamani H (2016) Fluoride removal from aqueous solutions by cupricoxide nanoparticles. *Fluoride* 49(3):233–244
- WHO (2006) Chemical fact sheets: fluoride, third ed., Guidelines for Drinking Water Quality (Electronic Resource): Incorporation First Addendum. Recommendations, vol. 1, WHO, Geneva, 375–377.
- Kagne S, Jagtap S, Dhawade Kamble SP, Devotta S, Rayalu SS (2008) Hydrated cement: a promising adsorbent for the removal of fluoride from aqueous solution. *J Hazard Mater* 154:88–95
- Balarak D, Mahdavi Y, Bazrafshan E, Mahvi AH, Esfandyari Y (2016) Adsorption of fluoride from aqueous solutions by carbon nanotubes: determination of equilibrium, kinetic, and thermodynamic parameters. *Fluoride* 49(1):71–83
- Kumar E, Bhatnagar A, Kumar U, Sillanpaa M (2011) Defluoridation from aqueous solutions by nano-alumina: Characterization and sorption studies. *J Hazard Mater* 186:1042–1049
- Meenakshi D, Maheshwari RC (2006) Fluoride in drinking water and its removal. *J Hazard Mater* 137(1):456–463
- Chen N, Zhang Z, Feng C, Sugiura N, Li M, Chen R (2010) Fluoride removal from water by granular ceramic adsorption. *Adv Colloid Interface Sci* 348:579–584
- Tembhurkar AR, Dongre S (2006) Studies on fluoride removal using adsorption process. *J Environ Sci Eng* 48:151–156
- Boldaji MR, Mahvi AH, Dobaradaran S, Hosseini SS (2009) Evaluating the effectiveness of a hybrid sorbent resin in removing fluoride from water. *Inter J Environ Sci Technol* 6(4):629–632
- Mahvi AH, Mostafapour FK, Balarak D, Khatibi AD. Adsorption of fluoride from aqueous solutions by a chitosan/zeolite composite. *Fluoride* 52(4):546–552.
- Zazouli MA, Mahvi AH, Mahdavi Y (2015) Isothermic and kinetic modeling of fluoride removal from water by means of the natural biosorbents sorghum. *Fluoride* 48(1):15–22
- Li YH, Wang S, Cao A, Zhao D, Zhang X, Xu C, Luan Z (2010) Adsorption of fluoride from water by amorphous alumina supported on carbon nanotubes. *Chem Phys Lett* 350:412–416
- Yu XL, Tong SR, Ge MF, Zuo JC (2013) Removal of fluoride from drinking water by cellulose-hydroxyapatite nanocomposites. *Carbohydr Polym* 92:269–275
- Mahvi AH, Mostafapour FK. Adsorption of fluoride from aqueous solution by eucalyptus bark activated carbon: thermodynamic analysis. *Fluoride* 52(4):562–568
- Al-Musawi TJ, Mahvi AH, Khatibi. Effective adsorption of ciprofloxacin antibiotic using powdered activated carbon magnetized by iron(III) oxide magnetic nanoparticles. *J Porous Mater.* 2021; 28, 835–852.
- Balarak D, Jaafari J, Hassani G, Agarwal, Gupta VK. The use of low-cost adsorbent (Canola residues) for the adsorption of methylene blue from aqueous solution: Isotherm, kinetic and thermodynamic studies. *Colloids Interface Sci. Commun.* 2015; 7, 16–19.
- Al-Musawi TJ, Mengelizadeh N, Taghavi M (2021) Activated carbon derived from Azolla filiculoides fern: a high-adsorption-capacity adsorbent for residual ampicillin in pharmaceutical wastewater. *Biomass Conv. Bioref.* <https://doi.org/10.1007/s13399-021-01962-4>
- Srivastav AL, Singh PK, Srivastava V, Sharma YC (2013) Application of a new adsorbent for fluoride removal from aqueous solutions. *J Hazard Mater* 263:342–352
- Haghighat GA, Dehghani MH, Nasseri S (2012) Comparison of carbon nanotubes and activated alumina efficiencies in fluoride removal from drinking water. *Indian J Sci Technol* 5(23):2432–2435
- Al-Musawi T, Mengelizadeh N, Ganji F, Wang C (2022) Preparation of multi-walled carbon nanotubes coated with  $\text{CoFe}_2\text{O}_4$  nanoparticles and their adsorption performance for Bisphenol A compound. *Adv Powder Technol* 33, 103438
- Yilmaz M, Al-Musawi TJ, Saloot Mk (2022) Synthesis of activated carbon from Lemna minor plant and magnetized with iron (III) oxide magnetic nanoparticles and its application in removal of Ciprofloxacin. *Biomass Conv. Bioref.* <https://doi.org/10.1007/s13399-021-02279-y>
- Al-Musawi TJ, Mengelizadeh N, Al Rawi O (2021) Capacity and Modeling of Acid Blue 113 Dye Adsorption onto Chitosan Magnetized by  $\text{Fe}_2\text{O}_3$  Nanoparticles. *J Polym Environ.* <https://doi.org/10.1007/s10924-021-02200-8>.
- Tran NBT, Duong NB (2021) Synthesis and Characterization of Magnetic  $\text{Fe}_3\text{O}_4$ /Zeolite NaA Nanocomposite for the Adsorption Removal of Methylene Blue Potential in Wastewater Treatment. *J Chem* 6678588.
- Khan TA, Khan EA, Shahjahan R (2015) Removal of basic dyes from aqueous solution by adsorption onto binary iron-manganese

- oxide coated kaolinite: non-linear isotherm and kinetics modeling. *Appl Clay Sci* 107:70–77
28. Rahmani A, Rahmani K, Dobaradaran S, Mahvi AH, Mohamad-jani R, Rahmani H (2010) Child dental caries in relation to fluoride and some inorganic constituents in drinking water in Arsanjan, Iran. *Fluoride* 43(4):179–186
  29. Somak C, Sirshendu D (2014) Adsorptive removal of fluoride by activated alumina doped cellulose acetate phthalate (CAP) mixed matrix membrane. *Sep Purif Technol* 125:223–238
  30. Bharali R, Bhattacharyya K, Krishna G (2015) Biosorption of fluoride on Neem (*Azadirachta indica*) leaf powder. *J Environ Chem Eng* 3(2):662–669
  31. Zhen J, Yong J, Kai-Sheng Z (2016) Effective removal of fluoride by porous MgO nanoplates and its adsorption mechanism. *J Alloy Compd* 675:292–300
  32. Sani T, Gómez-Hortigüela L, Perez-Pariente J, Chebude Y, Díaz I (2016) Defluoridation performance of nano-hydroxyapatite/stilbite composite compared with bone char. *Sep Purif Technol* 157:241–248
  33. Zúñiga-Muro NM, Bonilla-Petriciolet A, Mendoza-Castillo DI, Reynel-Ávila HE (2017) Fluoride adsorption properties of cerium-containing bone char. *J Fluor Chem* 197:63–73
  34. Çelik YH (2021) Characterization of Hazelnut, Pistachio, and Apricot Kernel Shell Particles and Analysis of Their Composite Properties. *J Nat Fibers* 18(7):1054–1068. <https://doi.org/10.1080/15440478.2020.1739593>
  35. Yami TL, Chamberlain JF, Butler EC, Sabatini DA (2016) Using a High-Capacity Chemically Activated Cow Bone to Remove Fluoride: Field-Scale Column Tests and Laboratory Regeneration Studies. *J Environ Eng* 143:04016083
  36. Leyva-Ramos R, Rivera-Utrilla J, Medellín-Castillo N, Sanchez-Polo M (2010) Kinetic modeling of fluoride adsorption from aqueous solution onto bone char. *Chem Eng J* 158:458–467
  37. Akbari H, Balarak D, Yousefi M, Rigi P, Mahvi AH. Fluoride removal from aqueous solution by almond shell activated carbon. *Fluoride*, 54(3), 269–282.
  38. Brunson LR, Sabatini DA (2009) An Evaluation of Fish Bone Char as an Appropriate Arsenic and Fluoride Removal Technology for Emerging Regions. *Environ Eng Sci* 26:1777–1783
  39. Loganathan P, Vigneswaran S, Kandasamy J, Naidu R (2013) Defluoridation of drinking water using adsorption processes. *J Hazard Mater* 248–249:1–19
  40. Wongrueng A, Sookwong B, Rakruam P, Wattanachira S (2016) Kinetic Adsorption of Fluoride from an Aqueous Solution onto a Dolomite Sorbent. *Eng J* 20:1–9
  41. Akbari H, Jorfi S, Mahvi AH, Yousefi M (2018) Adsorption of fluoride on chitosan in aqueous solutions: determination of adsorption kinetics. *Fluoride* 51(4):319–327
  42. Yadav KK, Gupta N, Kumar V, Khan S, Kumar A (2018) A review of emerging adsorbents and current demand for defluoridation of water: Bright future in water sustainability. *Environ Int* 111:80–108
  43. Kanouo BMD, Fonteh MF, Ngambo SP (2020) Development of a low cost household bone-char defluoridation filter. *Int J Biol Chem Sci* 14:1921–1927
  44. Zhijie Z, Yue T and Mengen Z (2011) Defluorination of wastewater by calcium chloride modified natural zeolite. *Desalination* 246–252.
  45. Erşan M, Bağcı E (2013) Investigation of kinetic and thermodynamic characteristics of removal of tetracycline with sponge like, tannin based cryogels. *Colloids Surf, B* 104:75–82
  46. Putra EK, Pranowoa, Sunarsob J, Indraswatia N, Ismadjia S (2009) Performance of activated carbon and bentonite for adsorption of amoxicillin from wastewater: mechanisms, isotherms and kinetics. *Water Res* 43, 2419–30.
  47. Sun Y, Fang Q, Dong J, Cheng X, Xu J (2011) Removal of fluoride from drinking water by natural stilbite zeolite modified with Fe(III). *Desalination* 277:121–127
  48. Balarak D, Mostafapour FK, Bazrafshan E, Mahvi AH (2017) The equilibrium, kinetic, and thermodynamic parameters of the adsorption of the fluoride ion on to synthetic nano sodalite zeolite. *Fluoride* 50(2):17–25
  49. Camacho LM, Torres A, Saha D, Deng S (2010) Adsorption equilibrium and kinetics of fluoride on sol-gel-derived activated alumina adsorbents. *Adv Colloid Interface Sci* 349:307–313
  50. Laura C, Lisa S, Decker D (2015) Comparing activated alumina with indigenous laterite and bauxite as potential sorbents for removing fluoride from drinking water in Ghana. *Appl Geochem* 56:50–66
  51. Fito J, Said H, Feleke S, Worku A (2019) Fluoride removal from aqueous solution onto activated carbon of *Catha edulis* through the adsorption treatment technology. *Environ Syst Res* 8:1–10
  52. Phillips O, Gupta DH, Mukhopadhyay BS, Gupta S (2018) Arsenic and fluoride removal from contaminated drinking water with Haix-Fe-Zr and Haix-Zr resin beads. *J Environ Manag* 215:132–142
  53. Mohan D (2011) Development of magnetic activated carbon from almond shells for trinitrophenol removal from water. *Chem Eng J* 172(2):1111–1125
  54. Foroutan R (2019) Performance of algal activated carbon/Fe<sub>3</sub>O<sub>4</sub> magnetic composite for cationic dyes removal from aqueous solutions. *Algal Res* 40:101509. <https://doi.org/10.1016/j.algal.2019.101509>
  55. Bhaumik R, Mondal NK, Das B, Roy P, Pal KC, J.K. Datta JK (2012) Eggshell powder as an adsorbent for removal of fluoride from aqueous solution: Equilibrium, kinetic and thermodynamic studies. *J Chem* 9; 1457–1480.
  56. Kennedy AM, Arias-Paic M (2020) Fixed-Bed Adsorption Comparisons of Bone Char and Activated Alumina for the Removal of Fluoride from Drinking Water. *J Environ Eng* 146:04019099
  57. Zazouli MA, Mahvi AH, Dobaradaran S, Barafrashtehpour M, Mahdavi Y (2014) Adsorption of fluoride from aqueous solution by modified Azolla Filiculoides. *Fluoride* 47(4):349–358
  58. Prabhu SM, Meenakshi S (2014) Synthesis of metal ion loaded silica gel/chitosan biocomposite and its fluoride uptake studies from water. *J Water Process Eng* 3:144–150
  59. Mourabet M, El-Boujaady H, El-Rhilassi A, Ramdane H, Ben-nani-Ziatni M (2011) Defluoridation of water using Brushite: equilibrium, kinetic and thermodynamic studies. *Desalination* 278:1–9
  60. Alhassan SI, Huang L, He Y, Yan L, Wu B, Wang H (2020) Fluoride removal from water using alumina and aluminum-based composites: A comprehensive review of progress. *Crit Rev Environ Sci Technol* 2020:1–35
  61. Song Z (2014) Synthesis and characterization of a novel MnOx-loaded biochar and its adsorption properties for Cu<sup>2+</sup> in aqueous solution. *Chem Eng J* 242:36–42. <https://doi.org/10.1016/j.cej.2013.12.061>
  62. Balarak D, Zafariyan M, Igwegbe CA (2021) Adsorption of Acid Blue 92 Dye from Aqueous Solutions by Single-Walled Carbon Nanotubes: Isothermal, Kinetic, and Thermodynamic Studies. *Environ Process* 8:869–888
  63. Al-Musawi TJ, Arghavan SMA, Allahyari E (2022) Adsorption of malachite green dye onto almond peel waste: a study focusing on application of the ANN approach for optimization of the effect of environmental parameters. *Biomass Conv. Bioref.* <https://doi.org/10.1007/s13399-021-02174-6>
  64. Dyanati-Tilaki RA, Yousefi Z, Yazdani-Cherati J (2013) The ability of azolla and lemna minor biomass for adsorption of phenol from aqueous solutions. *J Mazand Uni Med Sci* 23(106):140–146

**Publisher's note** Springer Nature remains neutral with regard to jurisdictional claims in published maps and institutional affiliations.